FlatChem 35 (2022) 100410

Contents lists available at ScienceDirect

FlatChem

journal homepage: www.sciencedirect.com/journal/flatchem

Inorganic graphenylene-like silicon carbide as anode material for Na batteries

Nicolas F. Martins [a], Guilherme S.L. Fabris [b], Ary S. Maia [c], Anderson R. Albuquerque [d], Julio R. Sambrano [a,*]

[a] Modeling and Molecular Simulation Group, São Paulo State University, 17033-360, Bauru, SP, Brazil
[b] Department of Materials Engineering, Federal University of Rio Grande do Norte, 59078-970, Natal, RN, Brazil
[c] Chemistry Department, Federal University of Paraíba, 58051-900, João Pessoa, PB, Brazil
[d] Chemistry Institute, Federal University of Rio Grande do Norte, 59078-970, Natal, RN, Brazil

ARTICLE INFO

Keywords:
SiC
Graphenylene
Sodium batteries
DFT
Adsorption

ABSTRACT

Sodium-based batteries are a viable alternative due to the abundance of Na in the environment and their higher sustainability compared to traditional lithium batteries. In this sense, density functional simulations were carried out to investigate the efficiency of the inorganic graphenylene-like silicon carbide (IGP-SiC), a semiconductor with a band gap energy of 3.22 eV, as a promising anode for sodium-based batteries, with a specific capacity of 610.46 mAh.g^{-1} and an atomic proportion of $Na_{1.92}SiC$ without the metal clustering process. Also is revealed that IGP-SiC exhibits conductive behavior with the first approximation of a Na atom. A range of 1.65 eV − 1.12 eV on Open-Circuit Voltage, an essential parameter in the commercial exploitation of batteries, was verified.

1. Introduction

Since the discovery of graphene[1], which has a wide range of technological applications[2–4], two-dimensional materials have received considerable attention. As expected, there has been an increase in interest in research into new alternatives to graphene, such as graphenylene (GP)[5,6], which is formed by carbon atoms symmetrically distributed in a periodic network of dodecagonal, hexagonal, and square rings. GP has opened up new possibilities for catalysis[7], gas separation [8], sensors[9], and as a promising anode in lithium[10] and sodium-[11] based batteries.

The current market difficulty for lithium use is the high costs and environmental problems associated with its extraction, in addition to the fact that its nature reserves are being depleted due to the need to meet the expansion and demand for the use of batteries in smartphones, notebooks, drones, electric and hybrid vehicles, and countless other electronic devices[12,13]. In this regard, there is an urgent need for new alternatives to diminish the problem of lithium use, as well as the development of new raw materials for use in batteries.

In the search for new alternatives, we highlight sodium[14,15], which is presented as a new option due to its abundance in nature and low extraction cost, facilitating production and reducing environmental impacts. Na atoms, on the other hand, have a larger radius, atomic mass, and redox potential than Li atoms[16,17], resulting in lower energy density and, as a result, a possible limitation in storage capacity. To mitigate the influence of this apparent negative impact on Na performance, an aluminum-based current collector can be used at the anode, which reduces the mass of the electrochemical cell and expands its energy efficiency while also producing less economic implications in manufacture compared to the traditional copper current collector[18].

For comparison, Yu[10] cites the promising application of GP as an anode material in Li batteries, with a ratio of one Li to two carbon atoms (Li_3C_6) and a theoretical specific capacity of 1116 mAh.g^{-1}, whereas the Na atomic proportion is $NaC_{1.5}$ with a theoretical specific capacity of 1459.77 mAh.g^{-1}[11]. In both cases, GP outperforms graphite (372 and 100 mAh.g^{-1} for Li/Na)[19,20], graphene/silicene heterostructure (487 mAh.g^{-1} for Li/Na)[21], phosphorene (434 and 324 mAh.g^{-1} for Li/Na) [22,23] and germanene (369 mAh.g^{-1} for Li/Na)[24], demonstrating the potential role of GP in energy storage.

Inorganic analogs of GP (IGP) have recently been investigated, including IGP-BN[25], IGP-Si[26], IGP-ZnO[27], and recently IGP-SiC [28], a semiconductor with an indirect band gap energy of 3.22 eV between the M and K points, which has promising multifunctionality as a toxic gas sensor, molecular sieving, and potential use in Na-based

* Corresponding author.
E-mail address: jr.sambrano@unesp.br (J.R. Sambrano).

https://doi.org/10.1016/j.flatc.2022.100410
Received 1 April 2022; Received in revised form 2 July 2022; Accepted 17 July 2022
Available online 20 July 2022

battery anodes[28] due to the facility of Na diffusion. Inspired by these properties, this study aims to demonstrate IGP-SiC as an anode for batteries.

The structural architecture of IGP-SiC is an important factor in maximizing Na storage, and it is from this that we estimate the Na adsorption configurations as well as the electronic and structural properties resulting from metal/foil interactions. Furthermore, the theoretical specific capacity is calculated to signal the energy efficiency of IGP-SiC by calculating the Open-Circuit Voltage (OCV), which is fundamental in understanding the charging and discharging processes[29].

2. Model system and computational details

The IGP-SiC unit cell belongs to the *P6/m* space group and contains 6 carbon atoms and 6 silicon atoms that form a hexagonal structure with lattice parameter $a = b = 8.35$ Å [28]. The IGP-SiC consists of dodecagonals, hexagonals, and square rings symmetrically distributed in a planar structure. The IGP-SiC unit cell is observed in Fig. 1I by the gray highlight.

The simulations were performed using the CRYSTAL17 software [30], and the density functional theory (DFT) applied to periodic systems, which is based on an expansion of the crystalline wave function to a set of localized Gaussian-type orbitals. Therefore, the B1WC hybrid functional [31] was combined with the triple-zeta valence polarization (TZVP) [32] basis set to describe the silicon and sodium atoms and the 6-311d11G [33] basis set for the carbon atoms. This methodology was used previously in Martins et al. [28].

The accuracy of the convergence criteria is determined by a set of five-threshold values set to 10^{-10}, 10^{-10}, 10^{-10}, 10^{-20}, and 10^{-40}. These parameters correspond respectively to the overlap and penetration for Coulomb integrals, the overlap for Hartree-Fock (HF) exchange integrals, and the last two thresholds for the pseudo-overlap in the HF exchange series. The shrinking factor (Pack–Monkhorst and Gilat net) was set to 20, corresponding to 68 independent k-points in the irreducible part of the Brillouin Zone.

All stationary points were characterized as a minimum (in functions of unit cell parameters and atomic coordinates) by diagonalizing the Hessian matrix with the Broyden-Fletcher-Goldfarb-Shanno (BFGS) algorithm for Hessian updating, using very tight criteria for the gradient convergence (10^{-4} a.u.) and nuclear displacements (4 x 10^{-4} a.u.) [34–36], and by analyzing the vibrational modes at the Γ point using the numerical second derivatives of total energies estimated with the coupled perturbed Hartree–Fock/Kohn–Sham algorithm [37–39].

A periodic 2x2 supercell containing 48 atoms (24Si and 24C atoms) was constructed, which permits accurate modeling of Na saturation on the IGP-SiC.

The periodic 2D symmetry (stacked sheets) of IGP-SiC is a crucial factor in metal adsorption. The homogeneous Na saturation above and below the structure optimizes the computational cost and reduces lattice distortions, increasing the material stability for anodic applications.

The total density of states (DOS) was analyzed using the Properties17 routine implemented in the CRYSTAL code, using the same k-point sampling method that was employed to diagonalize the Fock matrix during the optimization process.

The atomic interactions between Na-Na and Na-IGP-SiC were described by the Quantum Theory of Atoms in Molecules and Crystals [40], which performs the topological analysis of the electronic density, ρ(r), using the Topond code [41,42], implemented in the CRYSTAL package, and helps the understanding of the bond chemical character in the adsorption process. This analysis was based on the construction of 3D isosurface maps of the electron density (ρ(r)), the magnitude of the gradient of the electron density ($|\nabla\rho(r)|$), and the Laplacian of the electron density ($\nabla^2\rho(r)$), from a set of 20 to 50 perpendicular planes to the z-axis, for the pristine IGP-SiC, with one adsorbed Na atom and to the complete Na saturation of the IGP-SiC. The 3D isosurface maps were created using a Python script, supported by Plotly [43]. The atomic charges for all optimized adsorption models were obtained by the Bader charges.

In this sense, the evaluation of the adsorption process is followed by the adsorption energy (E_{ads}) calculation:

$$E_{ads} = \frac{(E_{IGP-SiC+Na} - E_{IGP-SiC} - N.E_{Na} + E_{BSSE})}{N} \quad (1)$$

where $E_{IGP-SiC+Na}$ is the supercell total energy of the IGP-SiC plus the

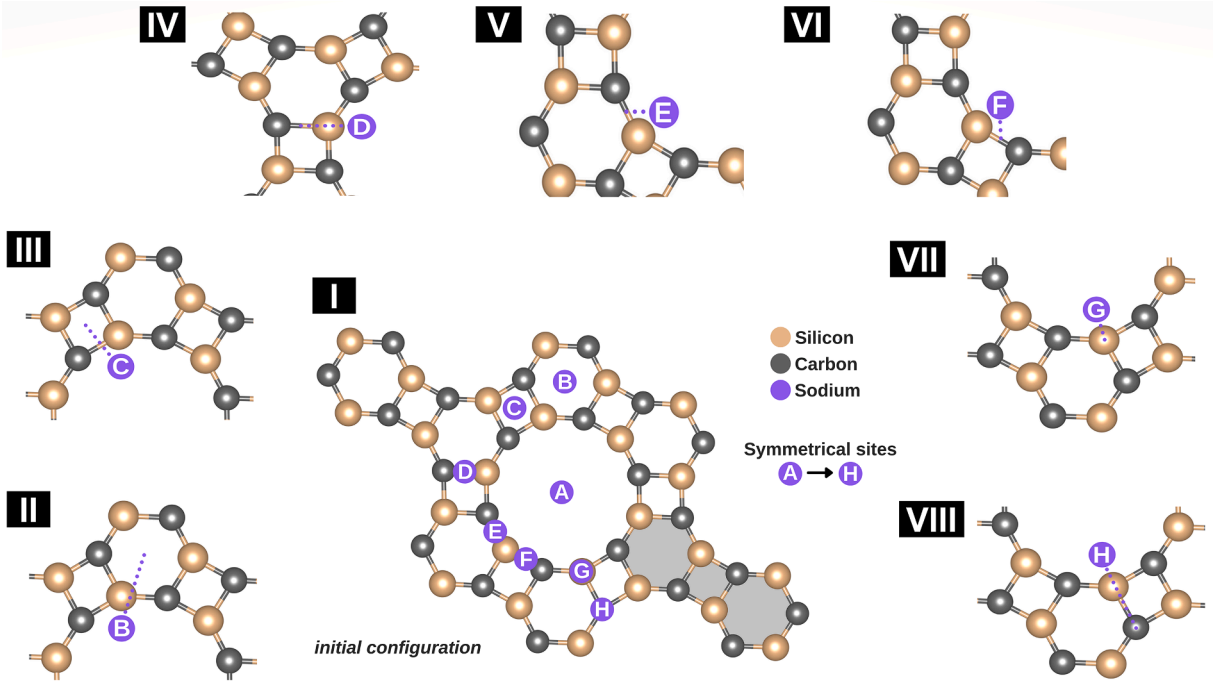

Fig. 1. (I) IGP-SiC (2x2) supercell with the initial high symmetrical sites for possible adsorption positions; (II to VIII) final configuration (after optimization) for sites B to H, respectively. The IGP-SiC unit cell is highlighted in gray color.

sodium atom, E_{Na} is the total energy of the isolated sodium atom, $E_{IGP-SiC}$ is the total energy of pristine IGP-SiC, and N is the number of Na atoms. The negative value of the adsorption energies indicates a favorable interaction between the IGP-SiC and the Na atoms, and the BSSE is the energy correction due to the basis set superposition error, calculated with *a posteriori* counterpoise method (CP) [44].

To calculate the energetic efficiency of the IGP-SiC, the theoretical storage capacity was estimated via Faraday's Law, where the capacity Q (in $mAh.g^{-1}$) is defined as.

$$Q = \frac{n_{Na}F}{3.6(n_{Na}m_{Na}+n_{Si}m_{Si}+n_{C}m_{C})} \quad (2)$$

where n_{Na}, n_{Si} e n_C are the numbers of sodium, silicon, and carbon atoms per cell, respectively, F is the Faraday's constant (9.648×10^4C/mol), and $m_{Na} = 23$u, $m_{Si} = 28$u, and e $m_C = 12$u are the sodium, silicon, and carbon atomic masses, respectively.

Furthermore, another important factor is the open-circuit voltage (OCV), which is an essential parameter in the performance of next-generation batteries and reveals the basic mechanisms of anode potential in electrochemical cells. The average (eV) is defined by.

$$OCV = -\frac{(E_{IGP-SiC+xNa} - E_{IGP-SiC} + E_{Na} + E_{BSSE})}{xnF} \quad (3)$$

where $E_{IGP-SiC+xNa}$ is the total supercell energy of IGP-SiC plus respective Na atomic concentration, n is the valence state of fully ionized Na atoms from the electrolyte ($n = 1$ for Na), and x is the atomic concentration, as assigned by Sun et al.[45] study. Since the OCV is the difference of electrical potential between the positive and negative terminals of a discharged battery, the negative sign is used in equation (3) to conserve the positive representation of the voltage profile.

To define paths for the commercial exploration of the IGP-SiC as an anode material, different stacking strategies of SiC and Na sheets were evaluated (Fig. 8) in focus on the storage capacity of the multi-layer IGP-SiC.

3. Results and discussions

Martins et al.[28] previously discussed the structural and electronic properties of IGP-SiC, with emphasis on the low barrier energy of Na diffusion in the central ring of IGP-SiC, which provides substantial mobility of Na atoms and thus favors its adsorption on both sides of IGP-SiC.

To comprehend the behavior of Na in IGP-SiC, the adsorption screened on high symmetric sites of a single Na atom was made based on the methodology reported previously by Fabris et al. [11], as shown in Fig. 1I: A, B, and C) centers of the rings, D, E, and F) between the rings and, G and H) up the silicon and carbon atoms, respectively.

It was demonstrated in the previous work[28] that the electron density is located at the border of the dodecagon (site A), which favors the spontaneous diffusion of the Na atoms, as shown in the electrostatic potential map of Fig. 3A.. At the same time, the other periodic rings (hexagons and squares) display a prohibitive energy barrier. Thus, the search for the minimum energy position for a single Na atom in sites B, C, D, E, F, G, and H reveals that they have shifted to a position near the silicon atoms, all with the same total energies (see Fig. 1(II) to 1(VIII)).

To understand the reason for the mobility of a single Na to be oriented close to the Si atoms of IGP-SiC, we performed a three-dimensional topological analysis evaluating different $|\nabla\rho(r)|$ and $\rho(r)$ isosurfaces, as shown in Fig. 2, which highlights that the adsorption of the Na atom occurs preferentially in the intermediate region between two carbon atoms, resulting in an apparent repulsion of the Si atom, which moves towards under the IGP-SiC structure. Furthermore, the single Na final configurations promote a change in the C-Si-C bond angles from 146° to ~ 119° due to Si displacement to the internal direction, changing the Si-C bonds from Si_1-$C_1 = 1.73$ Å and Si_1-$C_2 = 1.78$ Å to 1.83 and 1.88 Å, respectively.

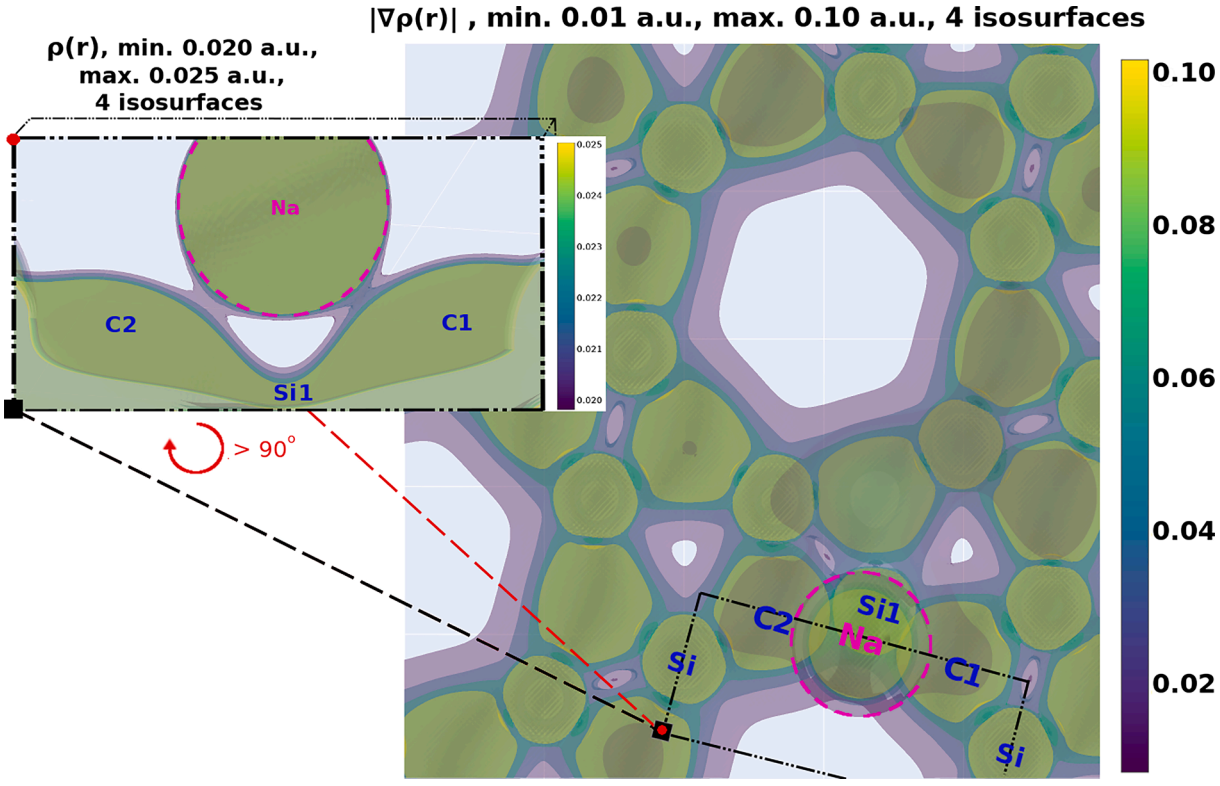

Fig. 2. Top view (xy-plane) of a 3D plot for a set of four $|\nabla\rho(r)|$ isosurfaces, with values between 0.01 and 0.1 a.u., highlighting the adsorption of a Na atom. Inset with a 3D plot for a set of four $\rho(r)$ isosurfaces, with values between 0.020 and 0.025 a.u., highlighting the adsorption of the Na atom by a rotation of the marked region.

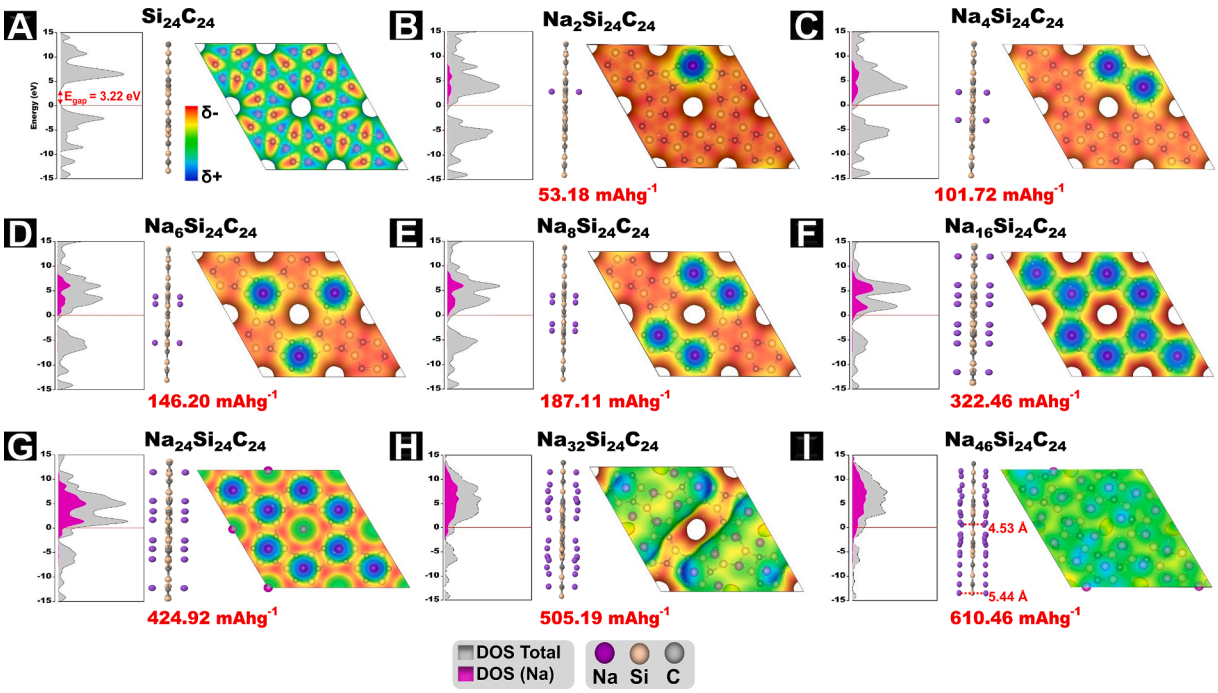

Fig. 3. (A-I) DOS, side view of each structure, top view of the electrostatic potential map [V(r)] (0.01 a.u isodensity), and storage capacity (in red color) of all considered configurations with an increasing concentration of Na atoms.

The inset in Fig. 2 shows four-electron density isosurfaces, ranging from 0.020 to 0.025 (a.u.), indicating that this is the maximum electron density range where interactions are observed between the adsorbed Na atom and the two neighboring C atoms, with no interaction detected with the Si atom, which underwent a downward deflection of the IGP-SiC structure.

Fig. 3 depicts a side view of IGP-SiC with increasing Na atom concentrations beyond the respective DOS. The electrostatic potential map on each DOS display also illustrates the top view of the Na interaction.

To understand the efficiency of this material, the specific capacity of each system was also evaluated.

The initial interaction occurred in the center of the hexagonal rings (site B in Fig. 1), with Na atoms adsorbed on both sides of IGP-SiC (Fig. 3B). Fig. 3(B) to 3(F) depict the process of Na occupation in the hexagons of the IGP-SiC supercell, where the top view (electrostatic potential maps) shows the absence of metal mobility, and the side configurations show structural stability after adsorption.

The inclusion of 4Na atoms in the central ring on both sides of the IGP-SiC modifies the electronic distribution of Na (Fig. 3G), with a density accumulation in all places of the structure and the symmetry playing an important role in this behavior. However, with the adsorption of Na atoms on the Si-C bonds at the edge of the central dodecagon (Fig. 3H), the mobility of the metals is directed towards the top of the carbon atoms, resulting in Na decongestion in IGP-SiC. Fig. 3I depicts the configuration of maximum Na atom storage in IGP-SiC ($Na_{46}Si_{24}C_{24}$), where the Na-Na dispersion causes greater mobility in all regions of the surface, not just around the carbon atoms, achieving an atomic ratio of 1.92Na atoms to one Si and one C, respectively ($Na_{1.92}SiC$).

The DOS shows that the IGP-SiC is a semiconductor with a band gap energy of 3.22 eV and acquires a conductive character in the presence of Na atom, demonstrating the influence of Na on the electronic properties of IGP-SiC. The change in electronic behavior is fundamental to the operation of an electrochemical cell because electrical conductivity promotes quick electronic mobility for the current collector, lowering electrical impedance and polarization during the charge and discharge process [47,48]. Furthermore, the IGP-SiC has thermal and dynamic stability at ~ 2100 K as shown in Fig. S1, indicating the plausibility of reproduction of the structure by experimentalists.

Fig. 3I also depicts the distances between two Na atoms symmetrically arranged on both sides of the IGP-SiC. The minimum and maximum Na distances are 4.53 Å and 5.44 Å, respectively, demonstrating the homogeneous behavior of the Na atoms when adsorbed on both sides of IGP-SiC.

Fig. 4 depicts the bonds between atom pairs in the Na_xSiC systems (x = 0,1,2, … 46), using only geometric distance criteria. Without Na atoms, the IGP-SiC has only three Si-C bond lengths (1.73, 1.78, and 1.83 Å), two in hexagonal rings and one in square rings. With the addition of Na atoms, some of these Si-C bonds have a slight tendency to elongate. In turn, the approximation of the Na atoms due to the increase in their concentration initially causes the Na-Na distances on opposite sides of the SiC plane to shorten (distances between 4.0 and 4.5 Å in Fig. 4(C) to 4(F)). The placement of two Na atoms in the central ring results in a connection of around 3 Å (Fig. 4G), which is shorter than the connections formed by Na positioned in the hexagons. Above 24Na atoms in the IGP-SiC supercell, lateral weakness between metals on the same plane face occurs, with a distribution in the range of 3 and 4 Å (Fig. 4H and 4I).

It should be noted that the tension of the rings artificially generates Si-Si connections (see the gray bar in Fig. 4A, at ~ 2.5 Å), which are mischaracterized as chemical bonds by topological analysis due to their lack of bond critical points (BCPs). The Supplementary Information (SI) contains additional information on the BCPs analysis of IGP-SiC bonds. Nonetheless, these and other connections were retained in Fig. 5 as structural descriptors.

Fig. 5 depicts the 3D maps of a set of four Laplacian ($\nabla^2\rho(r)$) isosurfaces, with a top view over the xy-plane, within a range of −0.5 to 0.5 a.u., contrasting the structure of pristine IGP-SiC with the structure with Na atoms adsorbed.

Here is assumed that negative Laplacian values of electron density are characteristic of local concentrations of the electron distribution, whereas positive values represent charge depletions [46]. Thus, in pristine IGP-SiC, silicon atoms have positive $\nabla^2\rho(r)$ values similar to Na and opposite to carbon atoms ($\nabla^2\rho(r) < 0$), which explains the

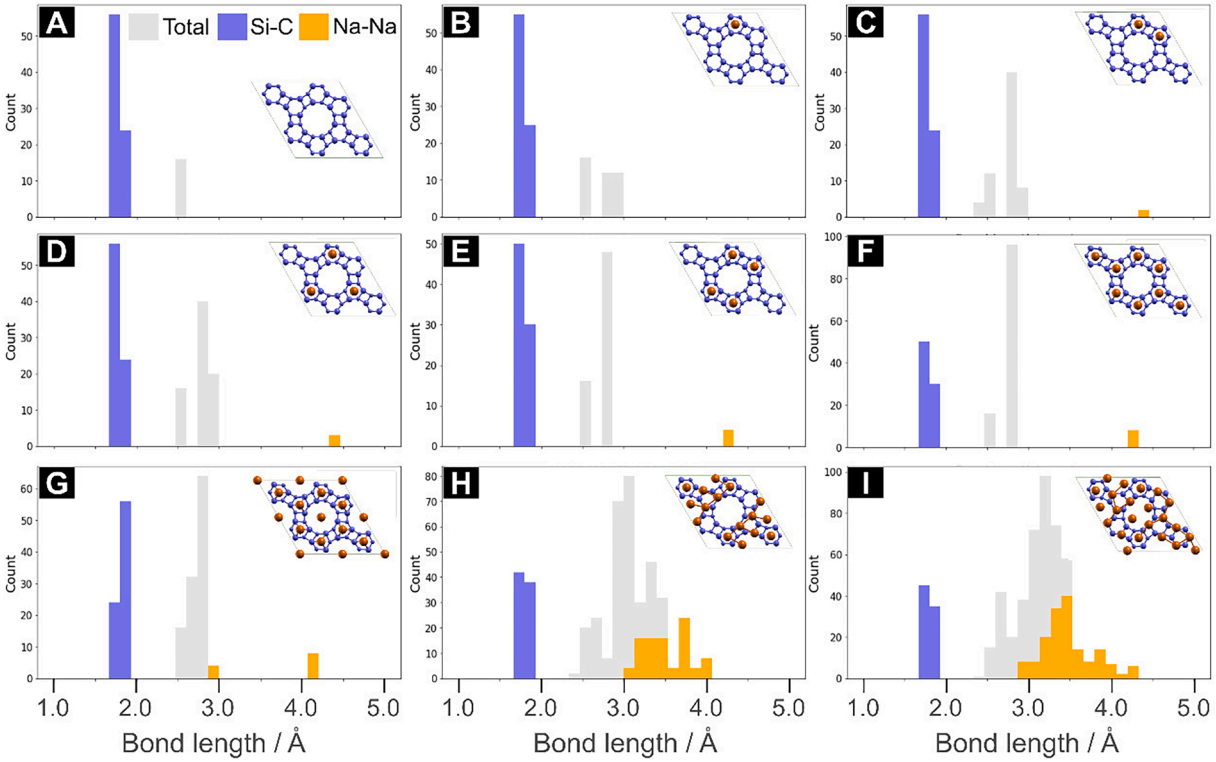

Fig. 4. Distribution of chemical bonds according to bond length (by purely geometric criterion). The violet bars indicate the Si-C bonds that form the 2D planes. The bonds between sodium atoms (Na-Na) are shown in orange. Bonds between all pairs of atoms are shown in gray. Structures (A) to (I) are systems with 0, 2, 4, 6, 8, 16, 24, 32, and 46Na atoms, symmetrically adsorbed on each side of the SiC plane. The graph scales on the ordinate axis (y) were adjusted based on the total number of connections.

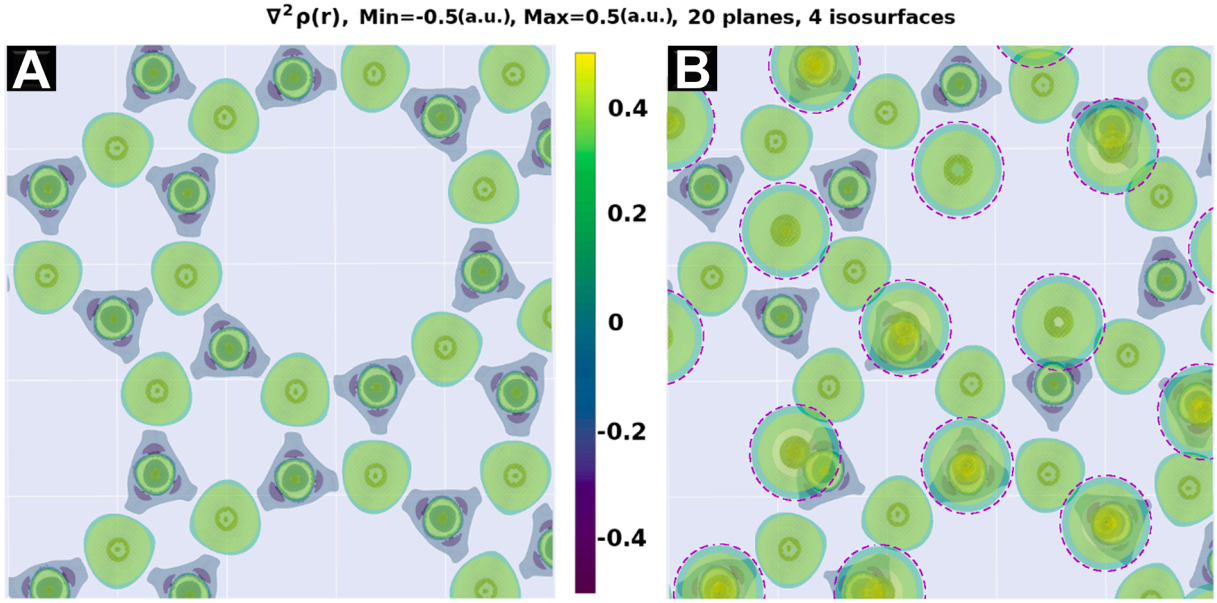

Fig. 5. Top view (xy plane) of a 3D plot for a set of four $\nabla^2\rho(r)$ isosurfaces, with values between −0.5 and 0.5 a.u., for the (A) pristine IGP-SiC and (B) the structure saturated with adsorbed Na atoms, highlighted in purple.

preferential positioning of Na adsorbed to C atoms or inside square and hexagonal rings, where they can interact with more than one carbon atom.

This finding supplements the previous one, which looked at the adsorption of a single sodium atom interacting with two adjacent carbon atoms (Fig. 2). In the case of single-atom adsorption, Na atoms have more freedom to interact with as many carbon atoms as possible (in this case, two), but the increase in the number of adsorbed Na atoms leads to greater targeting of these onto carbon atoms, as shown in Fig. 5B.

Fig. 6A elucidates the weak Na-Na interactions by showing that the adsorption energies become more negative as the metal concentration increases, reaching a value of −2.49 eV for the final saturation and indicating that the sodium atoms are linked to the IGP-SiC via physisorption. For the proposed application, the chemisorption process

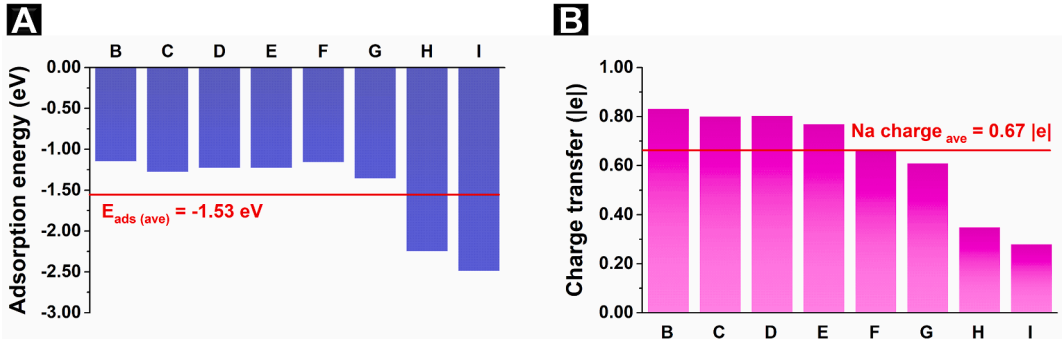

Fig. 6. (A) Adsorption energy and (B) Na charge transfer for each adsorption model of Fig. 3(B) to 3(I).

mustn't occur for the reason that chemical adsorption can change the structural and electronic properties of the Na and IGP-SiC system by forming a bond between the Na and the IGP-SiC.

The Bader charge analysis confirms the interaction between Na atoms and IGP-SiC (Fig. 6B), where an increase in Na saturation induces a charge transference from metal to the IGP-SiC structure, with a final configuration of 0.28 |e|.

The largest atomic proportion ($Na_{1.92}SiC$) reveals a specific capacity of 610.46 mAh.g^{-1} (1281.60 mAh.g^{-1}) for Na atoms, where the value in parentheses refers to the calculation without the Na mass, indicating that the IGP-SiC capacity is superior to graphite (100 mAh.g^{-1})[20], graphene/silicene heterostructure (476 mAh.g^{-1})[21] and graphene-based materials as phosphorene (324 mAh.g^{-1})[23] and germanene (369 mAh.g^{-1})[24].

Fig. 7 depicts the voltage profile of IGP-SiC as a function of the adsorbed Na atoms, which is an important factor in the electrochemical efficiency analysis. The OCV follows a standard decreasing trend as the concentration x of Na on the IGP-SiC surface increases, with a large drop in the curve when there is a variation from 2 atoms ($x = 0.083$ and 1.65 eV) to 4 atoms ($x = 0.167$ and 1.37 eV) of adsorbed Na atoms over IGP-SiC, and stabilizing at 1.17 eV ($x = 0.67$) with a plateau up to 1.12 eV for the $Na_{1.92}SiC$ system. This OCV profile is consistent with what is expected for battery applications, as it shows that the Na intercalation in the IGP-SiC is stable and the operating voltage is low (1.12 eV), which favors the increase of energy density and the behavior with commercial high voltage cathodes (charging and discharging process).

The study of the Na saturation on both sides of IGP-SiC allows for different stacking paths (Fig. 8), such as the sequence (Na-IGP-Na) - (…) - (…) - (Na-IGP-Na) built with a distance (Na-Na) of 3.5 Å (Fig. 8A), resulting in a ratio of $Na_{92}Si_{48}C_{48}$ ($Na_{1.92}SiC$) and a capacity of 610.46 mAh.g^{-1}, a value also observed for the final saturation of the Na adsorption study ($Na_{46}Si_{24}C_{24}$). Intercalation between the IGP-SiC and Na atoms can also be accomplished without the use of a deformation system (Fig. 8B), yielding a capacity of 526.82 mAh.g^{-1} for an atomic ratio of $Na_{69}Si_{48}C_{48}$ ($Na_{1.44}SiC$).

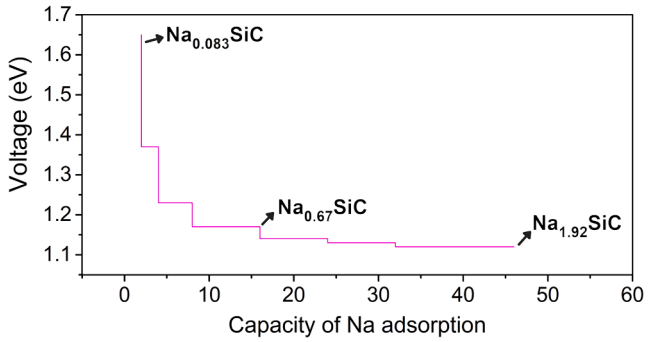

Fig. 7. Calculated voltage profile regarding Na adsorption.

The IGP-SiC and Na performance with more layers reveal the great performances of the system's final saturation when expanded in two different possibilities, indicating that the chosen sequence changes the specific capacity of the model because stacking with more Na layers (610.46 mAh.g^{-1}) is superior to IGP-SiC and Na intercalation (526.82 mAh.g^{-1}). Furthermore, when these new systems are expanded in *n*-arrangements, the specific capacity for each stacking model remains the same, indicating that the small-scale study of the anode potential of IGP-SiC ($Na_{46}Si_{24}C_{24}$) reproduces the identical behavior when configurations are enlarged into a universe of many atoms, reducing the computational and analysis costs incurred by researchers.

4. Conclusions

The interaction of Na atoms causes significant changes in the electronic behavior of IGP-SiC, making it conductive and suitable for anodic applications. However, because of the symmetrical balancing of the Na adsorbed atoms, the Na saturation does not affect the overall material's structure, resulting in more stable adsorptions as the Na amount increases.

As Na adsorption increases, the atoms migrate towards two C atoms of IGP-SiC, as demonstrated by electron density analysis, reinforcing that the preferred position of the Na atoms lies in the region of high interaction with carbon, where charge transfer between the Na atoms and IGP-SiC is observed. When the maximum atomic ratio of $Na_{1.92}SiC$ is reached, the theoretical specific capacity of 610.46 mAh.g^{-1} is obtained, indicating that IGP-SiC has high-efficiency energy when compared to other anode materials.

The open-circuit voltage profile, which exhibits a range of 1.67 eV – 1.12 eV as Na increases, attests to the low operating voltage and greater use facility of the SiC surface in electrodes, making IGP-SiC a promising anode material for Na batteries.

CRediT authorship contribution statement

Nicolas F. Martins: Conceptualization, Methodology, Software, Validation, Formal analysis, Writing – original draft, Writing – review & editing. **Guilherme S.L. Fabris:** Conceptualization, Methodology, Software, Validation, Formal analysis, Writing – original draft, Writing – review & editing. **Ary S. Maia:** Conceptualization, Methodology, Software, Validation, Formal analysis, Writing – original draft, Writing – review & editing. **A.R. Albuquerque:** Conceptualization, Methodology, Software, Validation, Formal analysis, Writing – original draft, Writing – review & editing. **Julio R. Sambrano:** Conceptualization, Funding acquisition, Investigation, Methodology, Project administration, Resources, Software, Supervision, Validation, Visualization, Writing – original draft, Writing – review & editing.

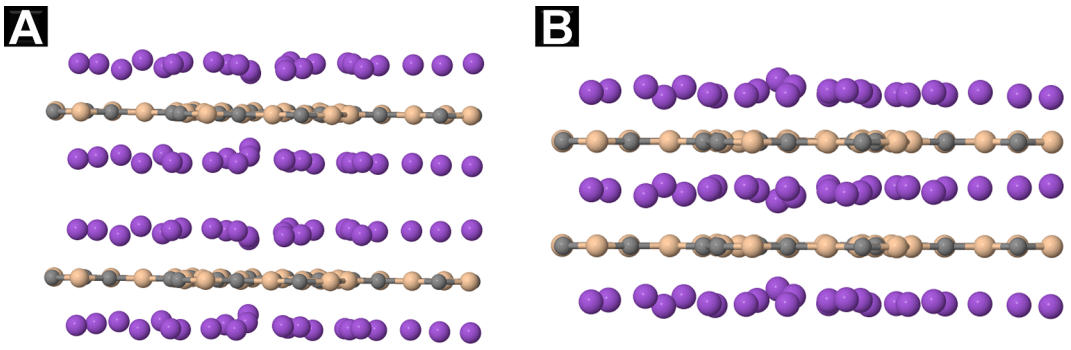

Fig. 8. Side view of geometries for (A) (Na-IGP-Na) - (…) - (…) - (Na-IGP-Na) with a $Na_{1.92}SiC$ ratio and (B) sodium-intercalated IGP-SiC with a $Na_{1.44}SiC$ ratio.

Declaration of Competing Interest

The authors declare that they have no known competing financial interests or personal relationships that could have appeared to influence the work reported in this paper.

Data availability

Data will be made available on request.

Acknowledgments

This work was supported by the Brazilian funding agencies FAPESP (2013/07296-2, 2019/08928-9, 2020/10380-9, 2022/00349-2, 2022/03959-6) CAPES - Finance Code 001 – (88887.467334/2019-00), and CNPq (grant no. 420062/2016-5, 421959/2016-9, 312854/2021-8, 307213/2021-8). The computational facilities were supported by resources supplied by the Molecular Simulations Laboratory (São Paulo State University, Bauru, Brazil) and High-Performance Computing Center (NPAD) at UFRN.

Appendix A. Supplementary data

Supplementary data to this article can be found online at https://doi.org/10.1016/j.flatc.2022.100410.

References

[1] A.K. Geim, K.S. Novoselov, The rise of graphene, Nat. Mater. 6 (2007) 183–191, https://doi.org/10.1038/nmat1849.
[2] T.-H. Han, H. Kim, S.-J. Kwon, T.-W. Lee, Graphene-based flexible electronic devices, Mater. Sci. Eng. R Reports. 118 (2017) 1–43, https://doi.org/10.1016/j.mser.2017.05.001.
[3] V. Dhinakaran, M. Lavanya, K. Vigneswari, M. Ravichandran, M.D. Vijayakumar, Review on exploration of graphene in diverse applications and its future horizon, Mater. Today Proc. 27 (2020) 824–828, https://doi.org/10.1016/j.matpr.2019.12.369.
[4] X.J. Lee, B.Y.Z. Hiew, K.C. Lai, L.Y. Lee, S. Gan, S. Thangalazhy-Gopakumar, S. Rigby, Review on graphene and its derivatives: Synthesis methods and potential industrial implementation, J. Taiwan Inst. Chem. Eng. 98 (2019) 163–180, https://doi.org/10.1016/j.jtice.2018.10.028.
[5] G. Brunetto, P.A.S. Autreto, L.D. Machado, B.I. Santos, R.P.B. dos Santos, D. S. Galvão, Nonzero gap two-dimensional carbon allotrope from porous graphene, J. Phys. Chem. C. 116 (2012) 12810–12813, https://doi.org/10.1021/jp211300n.
[6] V. Splugues, P.A.D.S. Autreto, D.S. Galvao, Hydrogenation dynamics of biphenylene carbon (Graphenylene) Membranes, MRS Adv. 2 (29) (2017) 1571–1576, https://doi.org/10.1557/adv.2017.239.
[7] W. Chen, Z. Wang, Y. Cui, Z. Li, Y. Li, X. Dai, Y. Tang, Graphenylene-supported single-atom (Ru and Mo) catalysts for CO and NO oxidations, New J. Chem. 44 (2020) 15733–15741, https://doi.org/10.1039/d0nj03842c.
[8] P. Rezaee, H.R. Naeij, Graphenylene–1 membrane: An excellent candidate for hydrogen purification and helium separation, Carbon N. Y. 157 (2020) 779–787, https://doi.org/10.1016/j.carbon.2019.10.064.
[9] Y. Tang, W. Chen, Z. Wang, G. Zhao, Y. Cui, Z. Li, Y.i. Li, Z. Feng, X. Dai, Formation, electronic, gas sensing and catalytic characteristics of graphene-like materials: A first-principles study, Appl. Surf. Sci. 530 (2020) 147178, https://doi.org/10.1016/j.apsusc.2020.147178.
[10] Y.X. Yu, Graphenylene: A promising anode material for lithium-ion batteries with high mobility and storage, J. Mater. Chem. A. 1 (2013) 13559–13566, https://doi.org/10.1039/c3ta12639k.
[11] G.S.L. Fabris, A.R. Albuquerque, R. Dovesi, J.R. Sambrano, A promising carbon-based nanosheet as a suitable Na-anode material, Mater. Sci. Eng. B Solid-State Mater. Adv. Technol. 268 (2021) 115121. https://doi.org/10.1016/j.mseb.2021.115121.
[12] P. Greim, A.A. Solomon, C. Breyer, Assessment of lithium criticality in the global energy transition and addressing policy gaps in transportation, Nat. Commun. 11 (2020) 1–11, https://doi.org/10.1038/s41467-020-18402-y.
[13] H. Bae, Y. Kim, Technologies of lithium recycling from waste lithium ion batteries: A review, Mater. Adv. 2 (2021) 3234–3250, https://doi.org/10.1039/d1ma00216c.
[14] C. Vaalma, D. Buchholz, M. Weil, S. Passerini, A cost and resource analysis of sodium-ion batteries, Nat. Rev. Mater. 3 (2018) 18013, https://doi.org/10.1038/natrevmats.2018.13.
[15] J.-Y. Hwang, S.-T. Myung, Y.-K. Sun, Sodium-ion batteries: present and future, Chem. Soc. Rev. 46 (2017) 3529–3614, https://doi.org/10.1039/C6CS00776G.
[16] K.M. Abraham, How comparable are sodium-ion batteries to lithium-ion counterparts? ACS Energy Lett. 5 (2020) 3544–3547, https://doi.org/10.1021/acsenergylett.0c02181.
[17] Y. Huang, Y. Zheng, X. Li, F. Adams, W. Luo, Y. Huang, L. Hu, Electrode materials of sodium-ion batteries toward practical application, ACS Energy Lett. 3 (2018) 1604–1612, https://doi.org/10.1021/acsenergylett.8b00609.
[18] E. Quartarone, T. Eisenmann, M. Kuenzel, C. Tealdi, A.G. Marrani, S. Brutti, D. Callegari, S. Passerini, Towards advanced sodium-ion batteries: green, low-cost and high-capacity anode compartment encompassing phosphorus/carbon nanocomposite as the active material and aluminum as the current collector, J. Electrochem. Soc. 167 (2020), 080509, https://doi.org/10.1149/1945-7111/ab856e.
[19] J.-M. Tarascon, M. Armand, Issues and challenges facing rechargeable lithium batteries, Nature. 414 (2001) 359–367, https://doi.org/10.1038/35104644.
[20] B. Jache, P. Adelhelm, Use of graphite as a highly reversible electrode with superior cycle life for sodium-ion batteries by making use of co-intercalation phenomena, Angew. Chemie Int. Ed. 53 (2014) 10169–10173, https://doi.org/10.1002/anie.201403734.
[21] L. Shi, T.S. Zhao, A. Xu, J.B. Xu, Ab initio prediction of a silicene and graphene heterostructure as an anode material for Li- and Na-ion batteries, J. Mater. Chem. A. 4 (2016) 16377–16382, https://doi.org/10.1039/C6TA06976B.
[22] S. Zhao, W. Kang, J. Xue, The potential application of phosphorene as an anode material in Li-ion batteries, J. Mater. Chem. A. 2 (2014) 19046–19052, https://doi.org/10.1039/C4TA04368E.
[23] X. Liu, Y. Wen, Z. Chen, B. Shan, R. Chen, A first-principles study of sodium adsorption and diffusion on phosphorene, Phys. Chem. Chem. Phys. 17 (2015) 16398–16404, https://doi.org/10.1039/C5CP02419F.
[24] B. Mortazavi, A. Dianat, G. Cuniberti, T. Rabczuk, Application of silicene, germanene and stanene for Na or Li ion storage: A theoretical investigation, Electrochim. Acta. 213 (2016) 865–870, https://doi.org/10.1016/j.electacta.2016.08.027.
[25] G.S.L. Fabris, N.L. Marana, E. Longo, J.R. Sambrano, Theoretical study of porous surfaces derived from graphene and boron nitride, J. Solid State Chem. 258 (2018) 247–255, https://doi.org/10.1016/j.jssc.2017.10.025.
[26] G.S.L. Fabris, N.L. Marana, E. Longo, J.R. Sambrano, Porous silicene and silicon graphenylene-like surfaces: a DFT study, Theor. Chem. Acc. 137 (2018), https://doi.org/10.1007/s00214-017-2188-6.
[27] G.S.L. Fabris, N.L. Marana, J.A.S. Laranjeira, E. Longo, J.R. Sambrano, New two-dimensional zinc oxide nanosheets: Properties, stability, and interconversion, Mater. Lett. 275 (2020), 128067, https://doi.org/10.1016/j.matlet.2020.128067.
[28] N.F. Martins, G.S.L. Fabris, A.R. Albuquerque, J.R. Sambrano, A new multifunctional two-dimensional monolayer based on silicon carbide, FlatChem. 30 (2021), 100286, https://doi.org/10.1016/j.flatc.2021.100286.
[29] I. Snihir, W. Rey, E. Verbitskiy, A. Belfadhel-Ayeb, P.H.L. Notten, Battery open-circuit voltage estimation by a method of statistical analysis, J. Power Sources. 159 (2006) 1484–1487, https://doi.org/10.1016/j.jpowsour.2005.11.090.
[30] R. Dovesi, A. Erba, R. Orlando, C.M. Zicovich-Wilson, B. Civalleri, L. Maschio, M. Rérat, S. Casassa, J. Baima, S. Salustro, B. Kirtman, Quantum-mechanical

condensed matter simulations with CRYSTAL, Wiley Interdiscip. Rev. Comput. Mol. Sci. 8 (2018) 1–36, https://doi.org/10.1002/wcms.1360.
[31] D.I. Bilc, R. Orlando, R. Shaltaf, G.M. Rignanese, J. Íñiguez, P. Ghosez, Hybrid exchange-correlation functional for accurate prediction of the electronic and structural properties of ferroelectric oxides, Phys. Rev. B - Condens. Matter Mater. Phys. 77 (2008) 1–13, https://doi.org/10.1103/PhysRevB.77.165107.
[32] M.F. Peintinger, D.V. Oliveira, T. Bredow, Consistent Gaussian basis sets of triple-zeta valence with polarization quality for solid-state calculations, J. Comput. Chem. 34 (2013) 451–459, https://doi.org/10.1002/jcc.23153.
[33] L. Valenzano, F.J. Torres, K. Doll, F. Pascale, C.M. Zicovich-Wilson, R. Dovesi, Ab initio study of the vibrational spectrum and related properties of crystalline compounds; the case of CaCO3 calcite, Zeitschrift Fur Phys, Chemie. 220 (2006) 893–912, https://doi.org/10.1524/zpch.2006.220.7.893.
[34] M. Ferrero, M. Rérat, R. Orlando, R. Dovesi, The calculation of static polarizabilities of 1–3D periodic compounds. the implementation in the crystal code, J. Comput. Chem. 29 (2008) 1450–1459, https://doi.org/10.1002/jcc.20905.
[35] M. Ferrero, M. Rérat, B. Kirtman, R. Dovesi, Calculation of first and second static hyperpolarizabilities of one- to three-dimensional periodic compounds. Implementation in the <scp>CRYSTAL</scp> code, J. Chem. Phys. 129 (2008), 244110, https://doi.org/10.1063/1.3043366.
[36] M. Ferrero, M. Rérat, R. Orlando, R. Dovesi, Coupled perturbed Hartree-Fock for periodic systems: The role of symmetry and related computational aspects, J. Chem. Phys. 128 (2008) 014110. https://doi.org/10.1063/1.2817596.
[37] C.G. Broyden, The Convergence of a Class of Double-rank Minimization Algorithms 1. General Considerations, IMA J. Appl. Math. 6 (1970) 76–90, https://doi.org/10.1093/imamat/6.1.76.
[38] R. Fletcher, A new approach to variable metric algorithms, Comput. J. 13 (1970) 317–322, https://doi.org/10.1093/comjnl/13.3.317.
[39] D. Goldfarb, A family of variable-metric methods derived by variational means, Math. Comput. 24 (1970) 23–23. https://doi.org/10.1090/S0025-5718-1970-0258249-6.
[40] R.F.W. Bader, H. Essén, The characterization of atomic interactions, J. Chem. Phys. 80 (1984) 1943–1960, https://doi.org/10.1063/1.446956.
[41] C. Gatti, S. Casassa, User's Manual (2017). https://www.crystal.unito.it/topond/topond.php.
[42] C.F. Matta, R.J. Boyd, in: An introduction to the Quantum Theory of Atoms in Molecules, Wiley, Weinheim, Germany, 2007, pp. 1–34, https://doi.org/10.1002/9783527610709.
[43] Plotly Technologies Inc, Collaborative data science, (2015). https://plot.ly.
[44] F.B. van Duijneveldt, J.G.C.M. van Duijneveldt-van, J.H. de Rijdt, van Lenthe, State of the art in counterpoise theory, Chem. Rev. 94 (1994) 1873–1885, https://doi.org/10.1021/cr00031a007.
[45] Q. Sun, Y. Dai, Y. Ma, T. Jing, W. Wei, B. Huang, Ab initio prediction and characterization of Mo2C monolayer as anodes for lithium-ion and sodium-ion batteries, J. Phys. Chem. Lett. 7 (2016) 937–943, https://doi.org/10.1021/acs.jpclett.6b00171.
[46] C. Gatti, V.R. Saunders, C. Roetti, Crystal field effects on the topological properties of the electron density in molecular crystals: The case of urea, J. Chem. Phys. 101 (1994) 10686–10696, https://doi.org/10.1063/1.467882.